HHS Public Access

Author manuscript

IEEE Trans Microw Theory Tech. Author manuscript; available in PMC 2017 April 01.

Published in final edited form as:

IEEE Trans Microw Theory Tech. 2016 April ; 64(4): 1339–1347. doi:10.1109/TMTT.2016.2536021.

Analyzing Single Giant Unilamellar Vesicles With a Slotline-Based RF Nanometer Sensor

Yan Cui,
Department of Electrical and Computer Engineering, Clemson University, SC 29634, USA

Anne K. Kenworthy,
Department of Molecular Physiology and Biophysics, Vanderbilt University Medical Center, Nashville, Tennessee 37232, USA

Michael Edidin,
Department of Biology, Johns Hopkins University, Baltimore, Maryland 21218, USA

Ralu Divan,
Center for Nanoscale Materials, Argonne National Laboratory, Argonne, IL 60439 USA

Daniel Rosenmann, and
Center for Nanoscale Materials, Argonne National Laboratory, Argonne, IL 60439 USA

Pingshan Wang
Department of Electrical and Computer Engineering, Clemson University, SC 29634, USA

Abstract

Novel techniques that enable reagent free detection and analysis of single cells are of great interest for the development of biological and medical sciences as well as point-of-care health service technologies. Highly sensitive and broadband radio-frequency (RF) sensors are promising candidates for such a technique. In this work, we present a highly sensitive and tunable RF sensor, which is based on interference processes and built with a 100 nm slotline structure. The highly concentrated RF fields, up to ~1.76×10^7 V/m, enable strong interactions between Giant unilamellar vesicles (GUVs) and fields for high sensitivity operations. We also provide two modeling approaches to extract cell dielectric properties from measured scattering parameters. GUVs of different molecular compositions are synthesized and analyzed with the RF sensor at ~2 GHz, ~2.5 GHz, and ~2.8 GHz with an initial $|S_{21}|_{min}$ of ~−100 dB. Corresponding GUV dielectric properties are obtained. A one-dimensional scanning of single GUV is also demonstrated.

Keywords

Complex dielectric permittivity; microwave sensor; microfluidics; giant unilamellar vesicles; conformal mapping

Phone: 864-6562117; fax: 864-6567220, pwang@clemson.edu.

I. Introduction

Reagent-free detection and analysis of single biological cells in solution at low cost are important for the development of biology, medicine, and point-of-care (POC) service [1]–[3]. Hence, reagent-free sensing and identification of the molecular composition and structure of cell membranes and organelles as well as cell cytoplasmic matrix are of great interest. Nevertheless, these goals are still elusive partly due to the lack of techniques sensitive enough to obtain such information.

Optical methods, which have dominated whole cell studies, are usually not sensitive enough to be used label-free, though stimulated Raman scattering (SRS) microscopy of single cells has been reported [4]. Additionally, optics is not compatible with complementary metal-oxide-semiconductor (CMOS) processes, which enable inexpensive and easy to use electronic systems. Therefore, various electrical approaches have been actively pursued to characterize the physical properties of single cells, identify the potential electrical markers of the cells and develop high-performance electronic systems for reagent-free analysis of the cells. Dielectric spectroscopy (DS) [1], usually referred to as impedance spectroscopy [1] at low-frequencies, emerges as a primary technique with significant progress, including label-free monitoring of stem cell differentiation [5], label-free analysis of leukocyte subpopulations [6] and of cancer cells [7]. However, most DS efforts, as well as electromechanical methods that also exploit cell electrical properties (e.g., electrophoresis (DEP) and electrorotation [8], [9]), operate at relatively low frequencies. High frequencies are expected to be necessary to probe cell interiors [10], [11] while broad frequency coverage is essential to uncover cell characteristics.

Unfortunately, DS sensitivity is often compromised at high frequencies [1]. The use of resonators [12], [13] and interferometers [14], [15] helps address this issue, but at single frequency points. Broadband [16] and multiple frequency DS [17] are reported with single cell sensitivities. These techniques require immobile cells. Recently, we have developed radio-frequency (RF) sensors of different forms with very high and tunable sensitivity over wide frequency ranges [18]–[21]. These sensors promise to be effective tools for the characterization and examination of single cells. In this work, we report our efforts on the design and operation of an RF interferometer that is based on nanometer slotlines (NSLs). NSLs strongly concentrate RF fields and improve interferometer sensitivity. We apply the interferometer as well as data extraction algorithms, which are developed in this work, to characterizing giant unilamellar vesicles (GUVs) of defined compositions.

GUVs are biologically relevant models that are often used to study cell membrane structures, such as liquid rafts and microdomains [22], [23]. They are also used to study cells, such as red blood cells [24]–[26]. GUV molecular compositions and interior solutions can be controlled and GUV domain structures are well documented. Thus, GUVs are a good model system for cell sensor examinations. We find that we can detect GUV over a range of GHz frequencies and that complex permittivities of GUV extracted from measured S-parameters imply differences in membrane organization among GUVs of different lipid compositions.

The remainder of the paper is arranged as follows: Section II discusses RF sensor design; Section III presents algorithms for extracting RF permittivity from measured *S*-parameters; Section IV describes GUV synthesis and measurement results; Section V presents our discussions and conclusions.

II. Slotline-based RF Sensor Design

Figure 1(a) shows the schematic of the RF sensor. Similar to the highly sensitive and tunable RF interferometers in [18]–[21], two broadband quadrature hybrids (QH) are used for RF probing signal division and combination. Off-chip tuning components, phase shifters (Φ) and attenuators (*R*), are introduced to tune the sensor sensitivity as well as the operating frequency. A slotline-based sensing structure, shown in Figs. 1(b) and 1(c), is used to probe single GUVs. Unlike coplanar waveguide transmission lines (CPWs) used in [18]–[21], slotlines are designed to yield higher RF fields for the same gap dimension w (Fig. 1(c)), which is often limited by fabrication techniques. Thus, stronger interactions between RF fields and GUVs [27] can be obtained for higher sensor sensitivities. Furthermore, better one-dimensional (1-D) spatial resolution can be achieved since a slotine has only one gap, unlike a CPW with two gaps and a signal line.

Baluns for nanometer slotline to CPW transitions [28] are shown in Fig. 1(a). CPWs are convenient for measurements. The RF structures, including the slotline and the baluns, are integrated on a fused-silica substrate through conventional micro-fabrication procedures. Lift-off processes are used for the deposition of Ti/Au (20 nm/200 nm) films. A focused ion beam (FIB) is used to form the 100 nm slotline. Figure 2 shows the simulated and measured performance of the RF structure around the designed center frequency, 3 GHz, around which the measurement will be performed. The simulation is conducted with High Frequency Structural Simulator (HFSS). Low return loss and insertion loss are achieved for sensor operations [21]. Factors that cause discrepancies between measurements and simulations include metal line dimension and cross-section deviations from layout, which is used for simulations. SMA female connectors and conductive epoxy used for measurement connection are also not taken into consideration in simulation.

Compared with our previous sensors that have millimeter (mm) and micrometer (μm) gaps [18]–[21], the RF electric fields of the 100 nm slotline are concentrated to achieve much stronger GUV-RF field interactions. Figure 3 depicts the electric field distribution at 3 GHz around the gap obtained with HFSS simulation. Minor asymmetry may be caused by simulation meshes, for which we used 0.5 μm as the maximum length of mesh elements due to a compromise between simulation accuracy and simulation time. For 5 dBm input power (used in our measurements), the electric field intensity is up to ~1.76×10^7 V/m around the sensing zone. In comparison, for the sensors with mm and μm gaps [18]–[21], the maximum electric field intensities are ~1.33×10^3 and ~1.73×10^5 V/m, respectively. Thus, the absolute sensitivity of the sensor is significantly improved, as illustrated by (22) and (24) below.

A polydimethylsiloxane (PDMS) microfluidic channel with a cross-section of 50 μm × 50 μm is built and incorporated with the slotline in the MUT branch, as shown in Fig. 4. The

GUV solution is injected into and extracted from the channel through two soft plastic tubes (not shown in Figs. 1 and 4) that are attached to the circular openings of the channel.

The introduction of a GUV particle, Fig. 1(c), will change the effective permittivity of the overall slotline structure and its *S*-parameters measured by the vector network analyzer (VNA). As a result, the particle properties can be obtained with the models presented in Sections III below.

III. GUV Dielectric Property Extraction

A. Conformal Mapping Method

The transmission *S*-parameter recorded by the VNA in Fig. 1(a) can be expressed as

$$S_{21,\mathrm{sol}}=\frac{\sqrt{2}}{2}e^{j0}K_1\frac{\sqrt{2}}{2}e^{j0}+\frac{\sqrt{2}}{2}e^{j\frac{\pi}{2}}K_2e^{-\gamma_{\mathrm{sol}}l_{\mathrm{sol}}}\frac{\sqrt{2}}{2}e^{j\frac{\pi}{2}}. \quad (1)$$

Subscript *sol* indicates solution. The propagation constant of the slotline section is γ_{sol} with a physical length of l_{sol}. The coefficients K_1 and K_2 describe the effects of all the other sensor components, including cables, attenuators and phase shifters. K_1 also includes the slotline, and can be measured independently using a calibrated VNA, as illustrated in Fig. 1(a). When a GUV flows above the slotline gap, the strong interaction between the electric field and GUV causes $|S_{21}|$ to be

$$S_{21,\mathrm{solp}}=\frac{\sqrt{2}}{2}e^{j0}K_1\frac{\sqrt{2}}{2}e^{j0}+\frac{\sqrt{2}}{2}e^{j\frac{\pi}{2}}K_2e^{-\gamma_{\mathrm{sol}}(l_{\mathrm{sol}}-l_{\mathrm{solp}})-\gamma_{\mathrm{solp}}l_{\mathrm{solp}}}\frac{\sqrt{2}}{2}e^{j\frac{\pi}{2}} \quad (2)$$

where the subscript *solp* is for solution with single GUV particle, as shown in Fig. 1(c). It is proved that for solutions with and without single GUV, which have close permittivity values, γ_{solp} can be solved using (1) and (2) when mismatches at the interfaces, as shown in Fig. 1(b), between microfluidic channel section of MUT/REF branch and transmission lines, are ignored [21]. For a solution with known permittivity, the propagation constant $\gamma_{sol}=\alpha_{sol}+j\beta_{sol}$ can be obtained from

$$\alpha_{\mathrm{sol}}=\frac{\pi}{\lambda_0}\frac{\varepsilon''_{\mathrm{eff,sol}}}{\sqrt{\varepsilon'_{\mathrm{eff,sol}}}} \quad (3)$$

$$\beta_{\mathrm{sol}}=\frac{2\pi f}{v_{\mathrm{ph}}}=\frac{2\pi f}{\sqrt{\varepsilon_0\varepsilon'_{\mathrm{eff,sol}}\mu_0}}. \quad (4)$$

The capacitance of a uniform slotline with the cross section shown in Fig. 1(c) can be approximated as the superposition of four partial capacitances C_{air}, C_{carr}, C_{sub} and C_{PDMS}, as shown in Fig. 5 [29]. Then, $\varepsilon'_{\text{eff}}$ and $\varepsilon''_{\text{eff}}$ can be obtained through,

$$\varepsilon'_{\text{eff,sol}}=\frac{C_{\text{air}}+C_{\text{sub}}(\varepsilon'_{\text{sub}})+C_{\text{carr}}(\varepsilon'_{\text{carr}})+C_{PDMS}(\varepsilon'_{PDMS})}{C_{\text{air}}} \quad (5)$$

$$\varepsilon''_{\text{eff,sol}}=\frac{C_{\text{carr}}(\varepsilon''_{\text{carr}})}{C_{\text{air}}} \quad (6)$$

where the subscript *sub* refers to the substrate, e.g., $\varepsilon'_{\text{sub}}=3.75$ for fused silica, while the subscript *carr* stands for the carrier solution of the particle. Only the dielectric loss coming from the solution is considered in (6). The expressions for the capacitances in (5) and (6) are

$$C_{\text{air}}=2\varepsilon_0\frac{K(k'_0)}{K(k_0)} \quad (7)$$

$$C_{\text{sub}}(\varepsilon_{\text{sub}})=\varepsilon_0(\varepsilon_{\text{sub}}-1)\frac{K(k'_{\text{sub}})}{K(k_{\text{sub}})} \quad (8)$$

$$C_{\text{carr}}(\varepsilon_{\text{carr}})=\varepsilon_0\varepsilon_{\text{carr}}\frac{K(k'_{\text{carr}})}{K(k_{\text{carr}})} \quad (9)$$

$$C_{PDMS}(\varepsilon_{PDMS})=\varepsilon_0(\varepsilon_{PDMS}-1)\frac{K(k'_{PDMS})}{K(k_{PDMS})}-\varepsilon_0\varepsilon_{PDMS}\frac{K(k'_{\text{carr}})}{K(k_{\text{carr}})}. \quad (10)$$

The functions K in (7)–(10) are incomplete elliptic integral of the first kind with variable $k_{0,sub,carr,PDMS}$ as

$$k_{0,\text{sub},\text{carr},PDMS}=\sqrt{\frac{2\tanh(0.5\pi w/h_{0,\text{sub},\text{carr},PDMS})}{1+\tanh(0.5\pi w/h_{0,\text{sub},\text{carr},PDMS})}} \quad (11)$$

where metal film thickness t is assumed to be negligible, w is the gap width of the slotline, $h_{sub,carr,PDMS}$ are thicknesses of substrate, solution and PDMS layers, and a semiempirical expression for the quasi-static non-frequency dependent approximation of distance h_0 is [29]

$$h_0 = h_{PDMS}\left(1+\frac{133}{2+\varepsilon'_{PDMS}}\right) \quad (12)$$

and $k' = (1-k^2)^{0.5}$.

The obtained $\gamma_{solp} = \alpha_{solp} + j\beta_{solp}$ from (1) and (2) is used to extract the complex permittivity of the particle, where the expression for α_{solp} and β_{solp} are the same as (3) and (4) with different subscripts. The partial capacitances in (5) and (6) have to be modified to include the dielectric and physical properties of single particles. As shown in Fig. 6, the carrier solution layer is split into upper and bottom layers (subscripts: *upp* and *bott*), and a particle-solution layer (subscript: *ps*), where we assume that the particle can be treated as a cylinder to acquire the unit length capacitance using the conformal mapping method. The validity of this assumption will be discussed at the third last paragraph of this sub-section. So $\varepsilon'_{\mathrm{eff,solp}}$ and $\varepsilon''_{\mathrm{eff,solp}}$ should be rewritten as

$$\varepsilon'_{\mathrm{eff,solp}} = \frac{C_{\mathrm{air}} + C_{\mathrm{sub}}(\varepsilon'_{\mathrm{sub}}) + C_{\mathrm{upp}}(\varepsilon'_{\mathrm{carr}}) + C_{ps}(\varepsilon'_p, \varepsilon'_{\mathrm{carr}}) + C_{\mathrm{bott}}(\varepsilon'_{\mathrm{carr}}) + C_{PDMS}(\varepsilon'_{PDMS})}{C_{\mathrm{air}}} \quad (13)$$

$$\varepsilon''_{\mathrm{eff,solp}} = \frac{C_{\mathrm{upp}}(\varepsilon''_{\mathrm{carr}}) + C_{ps}(\varepsilon''_p, \varepsilon''_{\mathrm{carr}}) + C_{\mathrm{bott}}(\varepsilon''_{\mathrm{carr}})}{C_{\mathrm{air}}} \quad (14)$$

where $\varepsilon'_p - j\varepsilon''_p$ is the complex permittivity of the particle, and the expressions for the capacitances, C_{upp} and C_{bott}, are

$$C_{\mathrm{upp}}(\varepsilon_{\mathrm{carr}}) = \varepsilon_0\varepsilon_{\mathrm{carr}}\left(\frac{K(k'_{\mathrm{carr}})}{K(k_{\mathrm{carr}})} - \frac{K(k'_{\mathrm{upp}})}{K(k_{\mathrm{upp}})}\right) \quad (15)$$

$$C_{\mathrm{bott}}(\varepsilon_{\mathrm{carr}}) = \varepsilon_0\varepsilon_{\mathrm{carr}}\frac{K(k'_{\mathrm{bott}})}{K(k_{\mathrm{bott}})}. \quad (16)$$

The variables k_{upp} and k_{bott} in (15) and (16) are

$$k_{\mathrm{upp}} = \sqrt{\frac{2\tanh(0.5\pi w/(SC+R))}{1+\tanh(0.5\pi w/(SC+R))}} \quad (17)$$

$$k_{\text{bott}}=\sqrt{\frac{2\ \tanh(0.5\pi w/(SC-R))}{1+\tanh(0.5\pi w/(SC-R))}} \quad (18)$$

where SC and R are the spherical-center coordinate and radius of the particle, respectively. It can be found from Fig. 6 that $h_{upp} = SC + R\ (\theta = \pi/2)$ and $h_{bott} = SC - R\ (\theta = -\pi/2)$ with θ shown in Fig. 6.

For the particle-solution layer, dielectrics in the mapped capacitance consist of two parts: particle and carrier solution, as shown in Fig. 7. Transforms (1) and (2) in [29] are used to map the particle-solution layer from z plane to w plane. Capacitance C_{ps} is in the form of

$$C_{ps}(\varepsilon_p,\varepsilon_{\text{carr}})=\int_{-\pi/2}^{\pi/2}\frac{K'\left(\sqrt{\frac{1-\tanh(0.5\pi(SC+R\sin\theta)/h_0)}{1+\tanh(0.5\pi(SC+R\sin\theta)/h_0)}}\right)d\theta}{K(k_0')}}{\frac{1}{\varepsilon_p\frac{K(k_x')}{K(k_x)}}+\frac{1}{\varepsilon_{\text{carr}}\left(\frac{K(k_0')}{K(k_0)}-\frac{K(k_x')}{K(k_x)}\right)}} \quad (19)$$

where $K'(f(\theta)) = \mathrm{d}(K(f(\theta)))/\mathrm{d}\theta$, and the coefficient k_x is also a function of the angle θ

$$k_x=\sqrt{\frac{2\ \tanh(0.5\pi\omega\ \tanh(0.5\pi R\cos\theta/(SC+R\sin\theta))/h_0)}{1+\tanh(0.5\pi\omega\ \tanh(0.5\pi R\cos\theta/(SC+R\sin\theta))/h_0)}}. \quad (20)$$

In (19), the terms $'(K(k_x')/K(k_x))^{-1'}$ and $'(K(k_0')/K(k_0)-\mathrm{K}(k_x')/K(k_x))^{-1'}$ represent the dielectric thicknesses for particle and solution, i.e., t_p and t_s in Fig. 7, respectively, corresponding to a given θ. Figure 8 shows normalized t_p and t_s versus θ (from $-\pi/2$ to $\pi/2$) for different SCs and Rs. The parameters for Case #0 in Fig. 8 will be used to extract complex permittivity in Section IV-C. Based on this, for Case #1 and #2 we changed R and w, respectively, to demonstrate their independent effect on t_p and t_s. Figure 8 shows that (*i*) the vertical position has a more significant effect than the radius through Case #0 and #1; (*ii*) the dielectric thickness in Fig. 7 increases with increased radius for the same vertical position through Case #1 and Case #2.

The GUV sphere is treated as a cylinder, which may cause significant errors, partly due to increased volume. A coefficient fitting factor $\kappa = 0.67$, which is also the volume ratio of the sphere and the approximated cylinder, is introduced to revise l_{solp} as $2\kappa R$.

Thus, the dielectric property of the measured particle can be obtained. Figure 9 summarizes the algorithm to obtain GUV permittivity values from S-parameters.

The conformal mapping method gives an intuitive and closed-form model for analyzing GUV permittivity from measured S-parameters. Yet, conformal mapping is rigorous for the analysis of two-dimensional direct-current (DC) systems or RF transverse-electromagnetic (TEM) systems. Although the slotline in Fig. 1 may be approximated as a quasi-TEM

system for the targeted frequency band, which is relatively narrow, GUVs are, in fact, three-dimensional objects. Therefore, the validity of the above model needs to be examined. This is accomplished by the experimental results presented in Section IV and by using a second modeling approach, discussed below.

B. Perturbation Method

We assume that the GUV particle in Fig. 1(c) only slightly perturbs the RF electric and magnetic fields of the slotline. Therefore, the un-perturbed RF fields can be used to calculate the interactions between the GUV and the RF fields. As a result, the new propagation constants of the slotline section, $\gamma_{sol,solp}$ in (1) and (2), can be obtained. So can the GUV properties. This assumption is reasonable since the RF properties of GUVs are expected to be close to those of the carrier liquids.

It is possible to obtain an approximate, closed-form analytical solution of slotline RF fields (without GUVs). The fields can also be obtained using simulation tools, such as COMSOL Multiphysics tools. The time cost of a single simulation is acceptable. Figure 10 shows the distributions of RF fields at the cross section in Fig. 1(c) with the dimensions given in Table I (only a part of the channel is shown), where ε_{carr}=76.05−*j*10.34 (glucose-water solution at 2.8 GHz [30]). The green circle indicates the location of a GUV, which is not included in the simulation for Fig. 10.

With the obtained RF field data and equations (2.17)–(2.20) in [27], equivalent circuit parameters *L, C, R* and *G* of the GUV loaded slotline can be obtained with a priori GUV properties. Corresponding $\gamma_{sol,solp}$ and *S*-parameters are obtained. This process is iterated with new GUV property values until the best match between the calculated and measured *S*-parameters is achieved. The time cost of this numerical iteration approach is significantly lower than that of full wave simulations of RF fields for each iteration step. The following are the main considerations.

The 10 μm diameter GUV sphere is divided into smaller elements, Fig. 11, which has 4,999 cubes with a side length of 0.5 μm, and 21 cubes along the diameter direction. A similar division is made for the carrier solution, not shown in Fig. 11.

Along the *z*-axis direction, there are 21 layers. For layer *i*, the corresponding parameters L_i, C_i, R_i and G_i can be calculated once their ε and μ are given.

$$L_i=\frac{1}{|I_0|^2}\left(\sum_{N_i}\mu_{N_i}|H_{xy}|^2\Delta S_{N_i}+\sum_{M_i}\mu_{M_i}|H_{xy}|^2\Delta S_{M_i}\right) \quad (21)$$

$$C_i=\frac{1}{|V_0|^2}\left(\sum_{N_i}\varepsilon'_{N_i}|E_{xy}|^2\Delta S_{N_i}+\sum_{M_i}\varepsilon'_{M_i}|E_{xy}|^2\Delta S_{M_i}\right) \quad (22)$$

$$R_i = \frac{R_S}{|I_0|^2} \sum_{T_i} |H_{xy}|^2 \Delta l_{M_i} \quad (23)$$

$$G_i = \frac{\omega}{|V_0|^2} \left(\sum_{N_i} \varepsilon''_{N_i} |E_{xy}|^2 \Delta S_{N_i} + \sum_{M_i} \varepsilon''_{M_i} |E_{xy}|^2 \Delta S_{M_i} \right) \quad (24)$$

where E_{xy} and H_{xy} are RF field intensities in the x-y plane, which are assumed to be uniform within one element; parameters Δl and ΔS are the length and area of one element; the subscript N_i describes a GUV element while subscript M_i for any non-GUV element, including solution, substrate, channel, PDMS, and air; parameter T_i is determined by the boundary lines on conductors in Fig. 1(c). In this example, Δl = 0.5 μm, ΔS = 0.25 μm^2, T_i=6,400 (two 800 μm long conductors), and for the first layer, N_1 = 37 (countable in Fig. 11), M_1 (channel part)=32,000−N_1=319,963 (for a 1600 μm × 50 μm channel); for other layers, N_i and M_i can also be found accordingly. The definitions for other parameters are the same as those in [27]. Then the propagation constant γ_i for each layer can be solved by $\gamma_i = \{(R_i + j\omega L_i)(G_i + j\omega C_i)\}^{0.5}$, and γ_{solp} in Section III-A for the microfluidic channel with single GUV can be considered as a set of γ_i. So the term $\gamma_{solp} l_{solp}$ in (2) can be expressed as

$$\gamma_{\mathrm{solp}} l_{\mathrm{solp}} = \sum_{i=1}^{21} \gamma_i \Delta l_i \quad (25)$$

where Δl_i is the length of layer i along the z-axis, e.g., 0.5 μm in this example.

The results from (25) are compared with measured results until the following conditions are satisfied with a set of ε_p:

$$|\mathrm{Re}(\gamma_{\mathrm{solp}} l_{\mathrm{solp}})_{\mathrm{measured}} - \mathrm{Re}(\gamma_{\mathrm{solp}} l_{\mathrm{solp}})_{\mathrm{calculated}}| < \delta \quad (26)$$

$$|\mathrm{Im}(\gamma_{\mathrm{solp}} l_{\mathrm{solp}})_{\mathrm{measured}} - \mathrm{Im}(\gamma_{\mathrm{solp}} l_{\mathrm{solp}})_{\mathrm{calculated}}| < \delta \quad (27)$$

where δ, e.g., 0.0001, represents the error tolerance.

In addition to extracting cell particle properties, the models above can also be used to rapidly predict the required $|S_{21}|_{min}$ for a given RF interferometer to measure a given particle using

$$|S_{21,\mathrm{solp}} - S_{21,\mathrm{sol}}| = |e^{-\gamma_{\mathrm{solp}} l_{\mathrm{solp}}} - e^{-\gamma_{\mathrm{sol}} l_{\mathrm{solp}}}|. \quad (28)$$

Table II summarizes the estimations for different dielectric properties, where we choose ε_{carr}=76.05−*j*10.34 (glucose-water solution at 2.8 GHz [30]), and ε_p is changed from 74.55−*j*11.84 to 10−*j*1. The other parameters are given in Table I. The results indicate reasonable agreement between HFSS full-wave simulation and model analysis. The effects of particle radius and vertical position on the required $|S_{21}|_{min}$ can also be evaluated. It should be pointed out that higher sensitivity (or lower $|S_{21}|_{min}$) in actual measurements is always required because of system losses (i.e., $|K_2|$< 1 in (2)) which is not considered in the above estimation.

For Model #2, the RF electric and magnetic fields, as shown in Fig. 10, are simulated without the GUV. In reality, the GUV tends to change the field distribution around it due to the dielectric property difference between the GUV and the carrier solution. So $|S_{21}|_{min}$ calculated using Model #2 is always lower than that using Model #1. Moreover, both Models #1 and #2 are based on the assumption of quasi-static TEM while HFSS is based on full-wave analysis. They tend to obtain different results.

The advantage of Model #2 is that there are no complex transformation expressions for conformal mapping, like (1) and (2) in [29]. The FEM-based direct-current (DC) simulation to obtain the electric and magnetic fields $|E|$ and $|H|$ is relatively easy, even for some more complex structures for which there are no transformation expressions for conformal mapping. However, no closed-form analytical expression is obtained for Model #2 to describe effect of every design parameter, e.g., *w*, h_{PDMS}, h_{sub}, and h_{carr} in Fig. 1.

IV. GUV Synthesis and RF Measurements

A. GUV Synthesis

We adopt the electroformation method [31] for GUV synthesis. Chol (Cholesterol), POPC (16:0-18:1 PC 1-palmitoyl-2-oleoyl-sn-glycero-3-phosphocholine) and SM (16:0 Egg Sphingomyelin) in chloroform are mixed at different mole fractions to form coexisting liquid-ordered phase L_o and liquid-disordered phase L_α (L_o + L_α) (Group *I*), liquid-ordered phase L_o (Group *II*), and liquid-disordered phase L_α (Group *III*) [32], as shown in Fig. 12 obtained with an epi-fluorescence microscope with an ET-FITC/CY3 Filter. Two fluorescent labels, Rho-PE(2-dioleoyl-sn-glycero-3-phosphoethanolamine- N-(lissamine rhodamine B sulfonyl) (ammonium salt)) and DioC18 (3,3'-Dioctadecyloxacarbocyanine Percholorate) are used for liquid-disordered phase L_α and liquid-ordered phase L_o domains, respectively. Three groups of GUV particles are synthesized with different molecular compositions (molar fraction) of POPC/SM/Chol: 2/1/1 (*I*), 1/2/2 (*II*), and 8/1/1 (*III*).

The main electroformation steps are the following. After dropping 80 μL Chol/lipids/labels mixture chloroform solution on a vacuum-desiccated indium tin oxide (ITO) glass, the liquid is spread out uniformly. Then, an O-ring rubber is placed on the glass, and sucrose-water solution at 0.1 M concentration level is dropped in the O-ring area, which is sealed to form a chamber using a second vacuum-desiccated ITO glass. The rubber-glass chamber is placed into an incubator at a miscibility transition temperature of ~60°C. A 1 V, 10 Hz sinusoidal wave is applied across the ITO electrodes. Lipid bilayers are formed. They will

spontaneously vesiculate in 2 hours. GUVs are then suctioned up from the chamber and dropped into 3 mL 0.1 M glucose-water solution for measurement.

B. RF Measurements of Single GUVs

Glucose-water solutions at a 0.1 M concentration level with GUV particles are first injected into the PDMS channel in Fig. 1. The sensor is tuned to a desired sensitivity at each target frequency f_0, i.e., a desired $|S_{21}|_{min}$ level before a GUV passes through the gap. Then a syringe pump is used to drive the GUV through the channel and the slotline gap. The solutions are in a laminar flow and potential swirls of the fluid in the channel contributing to possible tumbling motion of the GUV can be neglected. A fluorescent microscope is used to observe the labeled GUV simultaneously. The measurement setup is shown in Fig. 13. The GUV induced *S*-parameter changes are recorded by the VNA. The *S*-parameter will return to the initial $|S_{21}|_{min}$ after the GUV moves away from the slotline. Figure 14 shows two pairs (#1 and #2) of typical measurement results for Group *I* at ~2.8 GHz. In each of the pairs, both the initial and maximally changed (corresponding to the GUV right above the gap) $|S_{21}|$ are shown together. The value of $|S_{21}|_{min}$ and its corresponding frequency changes with time, i.e., GUV position, are shown in Fig. 15. The figures show that our sensor is capable of detecting a single GUV with good sensitivity. In Fig. 15, the maximum response occurs when the GUV appears above the gap. Multiple frequency measurements can be achieved to analyze GUV dielectric properties at different frequencies by adjusting phase shifters and attenuators. The initial $|S_{21}|_{min}$s are adjusted between ~−100 dB and ~−105 dB. The maximum responses are different for each set of GUV particles due to their different radii and vertical positions in the channel.

C. RF Dielectric Properties of Single GUVs

Figure 16 shows the extracted real and imaginary permittivity components of different GUV particles for each group at ~2 GHz, ~2.5 GHz, and ~2.8 GHz. Both models in Section III are used to obtain the permittivity values. The parameters for the calculations are listed in Table I. We choose 5 μm and 6 μm as the GUV radius and vertical center position, respectively. The 5 μm average GUV radius value is estimated by comparing GUVs with the 50 μm wide PDMS channel observed under microscope. From microscope observations, it is also estimated that these GUVs are close to the slotline surface because the microscope is focused on the surface plane before the GUVs pass through the gap. Then the measured *S*-parameters are recorded when a GUV is observed to be close to the surface. The error bars indicate the distributions of five repeated, but separate, measurements. In each group of the GUVs with the same compositions, the GUVs are synthesized and then measured on the same day. It shows that (*i*) the permittivity values of GUV particles are close to that of 0.1 M sucrose-water solution ($\varepsilon' - j\varepsilon'' = 82.87 - j7.83$ (at 2 GHz), $82.43 - j9.73$ (at 2.5 GHz), $82.12 - j10.85$ (at 2.8 GHz) through [33]), which is reasonable and serves to verify the validity of the proposed extraction method; (*ii*) roughly the same results are obtained using the proposed Model #1 and #2. The differences between the models have been further reduced with the use of $\kappa = 0.67$; (*iii*) the average ε' and ε'' also vary with frequencies, which may carry molecular dynamic process information. Further work is needed to understand the details.

The permittivity extraction and error range in Fig. 16 are from measuring five independent GUVs, which may have different diameters and vertical positions in the microfluidic channel. For each individual GUV particle, e.g., the one measured for Fig. 15, GUV size and vertical position are constant in the measurement process since the GUV only travels a very short distance. Using the measured *S*-parameters at each time moment (i.e., longitudinal location), the obtained GUV permittivity with Model #2 is shown in Table III. The almost identical GUV permittivity values, which are expected because GUV radius and vertical position do not induce relative error, further verify the validity of the model.

D. Discussion

The high intensity electric field of the nanometer slotline strongly interacts with GUV particles so that significant changes of S_{21} in magnitude and phase can be observed. High sensitivity operations enable high measurement accuracies, which are critical for detecting and observing subtle biological and physical processes in cells and GUVs as well as for identifying potential markers. Nevertheless, a few factors, such as the uncertainties of GUV radius, shape, and vertical position (i.e., h_{bott} in Fig. 6), need to be addressed in the future. The estimated effects of these factors are listed in Table IV. The data show that the GUV vertical position has more significant effects than the uncertain radius on the interaction.

Fig. 15 shows that the RF sensor can be used to perform a 1-D scanning of a GUV particle, hence, a biological cell in the future. The scanning process may be further investigated to provide GUV surface domain structure information at high spatial resolution (e.g., ~100 nm) since GUV vertical position can be approximated as a constant therein.

A potential issue with the system in Fig. 1 is the strong RF field effects on GUV lipids, e.g., thermal effect, which can be estimated by use of equations (2.95) in [27] and (3) in [34]. The results show a 432°C/*s* temperature change rate, which is probably not realistic. This needs to be explored in the future. In our measurement, we observed that GUV shapes do not change before and after passing though the slotline gap, which is consistent with the results in Fig. 15. Moreover, it was proved that the high fields do not damage GUVs (hence cells) appreciably [35].

V. Conclusions

We present an interferometer based RF sensor with 100 nm slotlines. The sensor is highly sensitive and tunable in both operating frequency and sensitivity. Models are established and verified to obtain the RF properties of particles in carrier solution from measured scattering parameters. GUVs with different molecular compositions are synthesized, tested and analyzed with the sensor. The results show that the sensor can detect and scan GUVs at multiple frequency points, and the average dielectric properties of the GUV particles extracted with the two models agree with each other reasonably well. It is expected that the sensor can be further developed, including measurement accuracy improvement, for GUV and cell investigations.

Acknowledgments

This work was supported by NIH 1K25GM100480-01A1. Use of the Center for Nanoscale Materials was supported by the U. S. Department of Energy, Office of Science, Office of Basic Energy Sciences, under Contract No. DE-AC02-06CH11357.

The authors appreciate Dr. C. A. Day, and Dr. P. J. Barrett, at Vanderbilt University for helping in GUV synthesis, and Dr. T. Darroudi at Clemson University for helping in FIB etching.

REFERENCES

1. Sun T, Morgan H. Single-cell microfluidic impedance cytometry: a review. Microfluid Nanofluid. 2010 Mar; 8(4):423–443.
2. Brehm-Stecher BF, Johnson EA. Single-cell microbiology: tools, technologies, and applications. Microbiol. Mol. Biol. Rev. 2004 Sep; 68(3):538–559. [PubMed: 15353569]
3. Liu Q, Wu C, Cai H, Hu N, Zhou J, Wang P. Cell-based biosensors and their application in biomedicine. Chem. Rev. 2014 Jun; 114(12):6423–6461. [PubMed: 24905074]
4. Freudiger CW, Min W, Saar BG, Lu S, Holtom GR, He C, Tsai JC, Kang JX, Xie XS. Label-free biomedical imaging with high sensitivity by stimulated Raman scattering microscopy. Science. 2008 Sep; 322(5909):1857–1861. [PubMed: 19095943]
5. Bagnaninchi PO, Drummond N. Real-time label-free monitoring of adipose-derived stem cell differentiation with electric cell-substrate impedance sensing. Proc. Natl. Acad. Sci. USA. 2011 Apr; 108(16):6462–6467. [PubMed: 21464296]
6. Holmes D, Pettigrew D, Reccius CH, Gwyer JD, van Berkel C, Holloway J, Davies DE, Morgan H. Leukocyte analysis and differentiation using high speed microfluidic single cell impedance cytometry. Lab Chip. 2009 Aug.9:2881–2889. [PubMed: 19789739]
7. Han A, Yang L, Frazier AB. Quantification of the heterogeneity in breast cancer cell lines using whole-cell impedance spectroscopy. Clin. Cancer. Res. 2007 Jan; 13(1):139–143. [PubMed: 17200348]
8. Yang J, Huang Y, Wang X, Wang X-B, Becker FF, Gascoyne PR. Dielectric properties of human leukocyte subpopulations determined by electrorotation as a cell separation criterion. Biophys. J. 1999 Jun; 76(6):3307–3314. [PubMed: 10354456]
9. Gossett DR, Weaver WM, Mach AJ, Hur SC, Tse HTK, Lee W, Amini H, Di Carlo D. Label-free cell separation and sorting in microfluidic systems. Anal. Bioanal. Chem. 2010 Apr; 397(8):3249–3267. [PubMed: 20419490]
10. Haandbæk N, Bürgel SC, Heer F, Hierlemann A. Characterization of subcellular morphology of single yeast cells using high frequency microfluidic impedance cytometer. Lab Chip. 2014 Oct. 14:369–377. [PubMed: 24264643]
11. Grenier K, Dubuc D, Chen T, Artis F, Chretiennot T, Poupot M, Fournié J. Recent advances in microwave-based dielectric spectroscopy at the cellular level for cancer investigations. IEEE Trans. Microwave Theory and Techn. 2013 May; 61(5):2023–2030.
12. Haandbæk N, Bürgel SC, Heer F, Hierlemann A. Resonance-enhanced microfluidic impedance cytometer for detection of single bacteria. Lab Chip. 2014 Jun; 14(17):3313–3324. [PubMed: 24984254]
13. Wood D, Oh S-H, Lee S-H, Soh H, Cleland A. High-bandwidth radio frequency Coulter counter. Appl. Phys. Lett. 2005 Oct.87(18):184106.
14. Ferrier GA, Romanuik SF, Thomson DJ, Bridges GE, Freeman MR. A microwave interferometric system for simultaneous actuation and detection of single biological cells. Lab Chip. 2009 Oct. 9:3406–3412. [PubMed: 19904408]
15. Yang Y, Zhang H, Zhu J, Wang G, Tzeng T-R, Xuan X, Huang K, Wang P. Distinguishing the viability of a single yeast cell with an ultra-sensitive radio frequency sensor. Lab Chip. 2010; 10:553–555. [PubMed: 20162228]
16. Ning Y, Multari C, Luo X, Palego C, Cheng X, Hwang JC, Merla C, Apollonio F, Liberti M. Broadband electrical detection of individual biological cells. IEEE Trans. Microw. Theory Techn. 2014 Sep; 62(9):1905–1911.

17. Chen T, Artis F, Dubuc D, Fournie J, Poupot M, Grenier K. Microwave biosensor dedicated to the dielectric spectroscopy of a single alive biological cell in its culture medium. IEEE MTT-S Int. Microw. Symp. 2013:1–4.
18. Cui Y, Sun J, He Y, Wang Z, Wang P. A simple, tunable, and highly sensitive radio-frequency sensor. Appl. Phys. Lett. 2013 Aug.103(6):062906.
19. Cui Y, He Y, Wang P. A quadrature-based tunable radio-frequency sensor for the detection and analysis of aqueous solutions. IEEE Microw. Wireless Compon. Lett. 2014 Jul; 24(7):490–492.
20. Cui Y, Li J, Cao W, Wang P. Highly sensitive RF detection and analysis of DNA solutions. IEEE MTT-S Int. Microw. Symp. 2014:1–4.
21. Cui Y, Wang P. The design and operation of ultra-sensitive and tunable radio-frequency interferometers. IEEE Trans. Microw. Theory Techn. 2014 Dec; 62(12):3172–3182.
22. Edidin M. The state of lipid rafts: from model membranes to cells. Annu. Rev. Biophys. Biomol. Struct. 2003 Jan.32:257–283. [PubMed: 12543707]
23. Day CA, Kenworthy AK. Tracking microdomain dynamics in cell membranes. Biochim. Biophys. Acta.-Biom. 2009 Nov; 1788(1):245–253.
24. Vlahovska PM, Podgorski T, Misbah C. Vesicles and red blood cells in flow: From individual dynamics to rheology. C. R. Physique. 2009 Nov; 10(8):775–789.
25. Vlahovska PM, Barthes-Biesel D, Misbah C. Flow dynamics of red blood cells and their biomimetic counterparts. C. R. Physique. 2013 Jun-Jul;14(6):451–458.
26. Li X, Vlahovska PM, Karniadakis GE. Continuum-and particle-based modeling of shapes and dynamics of red blood cells in health and disease. Soft Matter. 2013 Oct.9:28–37. [PubMed: 23230450]
27. Pozar, DM. Microwave Engineering. 4th. New York: Wiley; 2012. p. 50-52.p. 82
28. Simons, RN. Coplanar Waveguide Circuits, Components, and Systems. New York: Wiley; 2012. p. 331-332.
29. Svačina J. Dispersion characteristics of multilayered slotlines—a simple approach. IEEE Trans. Microwave Theory and Techn. 1999 Sep; 47(9):769–772.
30. Weingärtner H, Knocks A, Boresch S, Hochtl P, Steinhauser O. Dielectric spectroscopy in aqueous solutions of oligosaccharides: experiment meets simulation. J. Chem. Phys. 2001 Jul; 115(3): 1463–1472.
31. Angelova M, Dimitrov DS. A mechanism of liposome electroformation. Progr. Colloid Poymr. Sci. 1988; 76:59–67.
32. Ionova IV, Livshits VA, Marsh D. Phase diagram of ternary cholesterol/palmitoylsphingomyelin/palmitoyloleoylphosphatidylcholine mixtures: spin-label EPR study of lipid-raft formation. Biophys. J. 2012 Apr; 102(8):1856–1865. [PubMed: 22768941]
33. Reid, C. Ph.D. dissertation. London, UK: Dept. Medical Phys. Bioeng., Univ. College; 2009. Spectroscopic methods for medical diagnosis at terahertz wavelengths; p. 128-129.
34. Kharkovsky SN, Hasar UC. Measurement of mode patterns in a high-power microwave cavity. IEEE Trans. Instrum. Meas. 2003 Dec; 52(6):1815–1819.
35. Dimova R, Riske KA, Aranda S, Bezlyepkina N, Knorr RL, Lipowsky R. Giant vesicles in electric fields. Soft Matter. 2007 May.3:817–827.

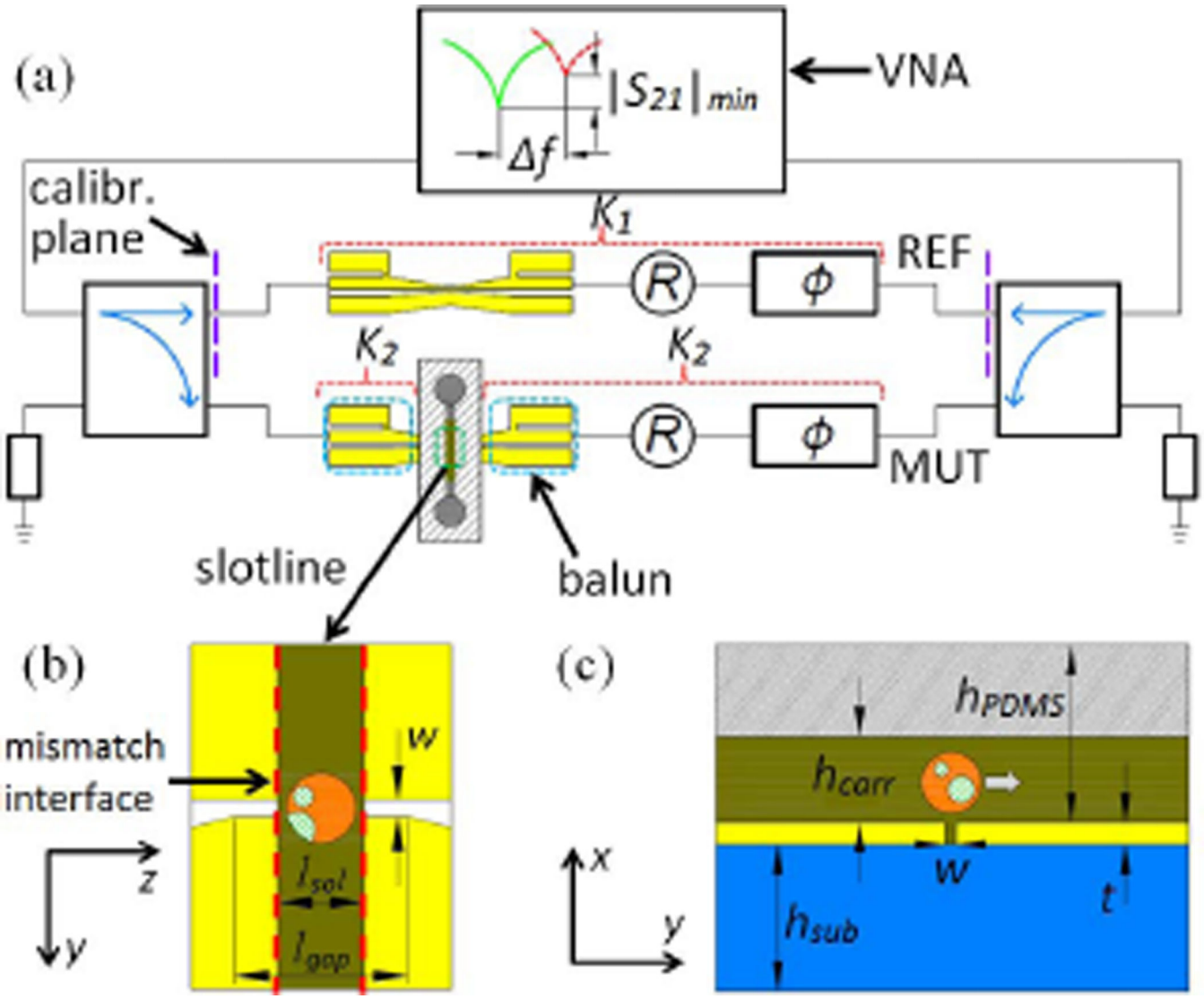

Fig. 1.

(a) Schematic of the RF sensor. (b) The top and (c) cross section views of the sensing zone in (a) with single GUV (circle), where dimensions w=100 nm (gap), t=220 nm (Ti/Au), h_{carr}=50 μm (channel height), h_{sub}=1 mm (substrate), h_{PDMS} =~2 mm (PDMS cover), l_{sol} = 50 μm (channel width), and l_{gap}=100 μm. The dimension for the CPW is 0.1 mm/1.5 mm/0.1 mm (gap/signal line/gap). Abbreviations MUT and REF represent material-under-test and reference branches, respectively. Coefficients K_1, K_2 will be used to describe effects of indicated components. Φ and R represent phase shifters and attenuators, respectively. The Cartesian coordinate systems are marked for (b) and (c). The mismatch interfaces for impedance are marked by red dash lines in (b).

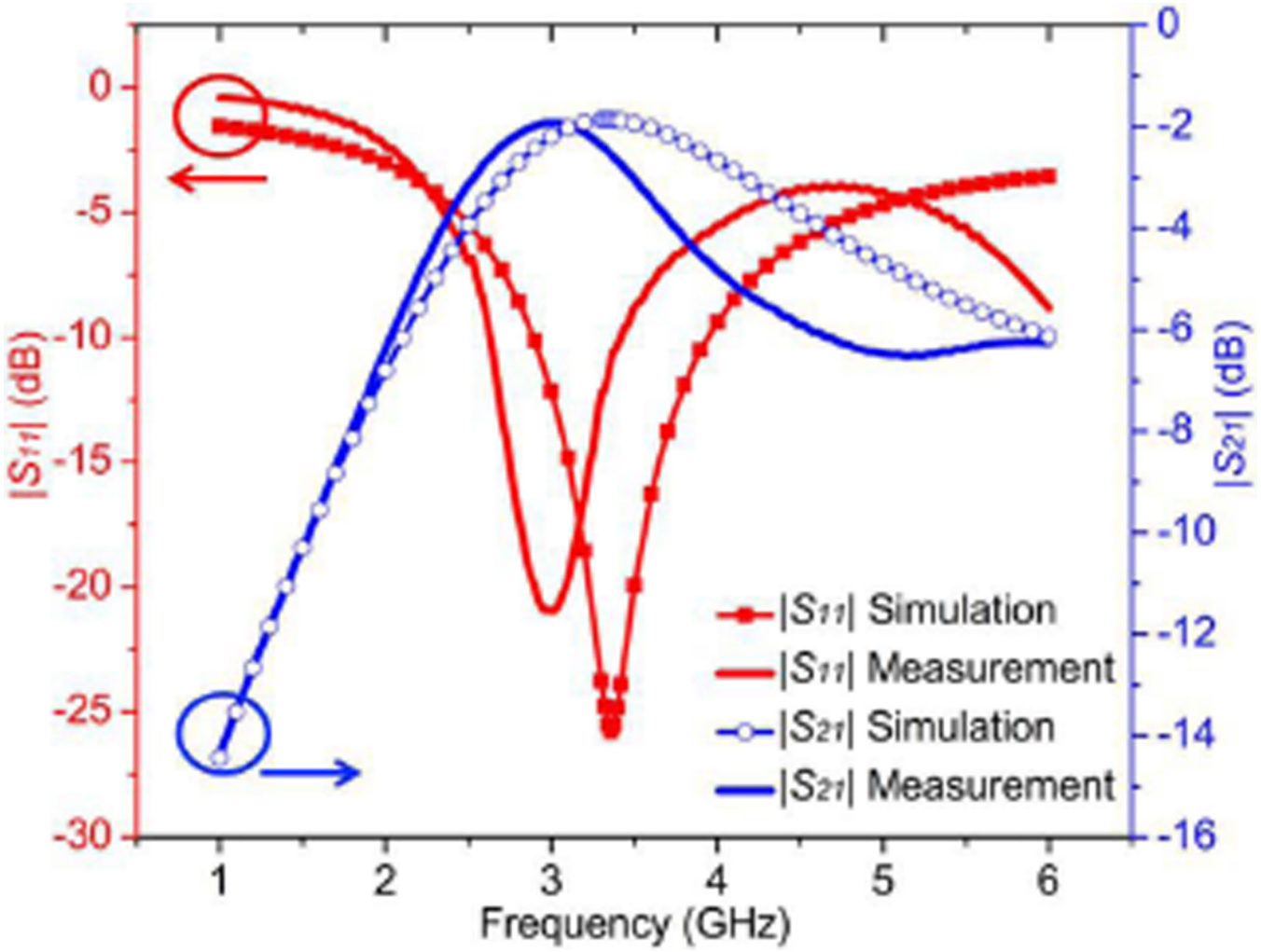

Fig. 2.
S-parameters of the nanometer RF sensing structure.

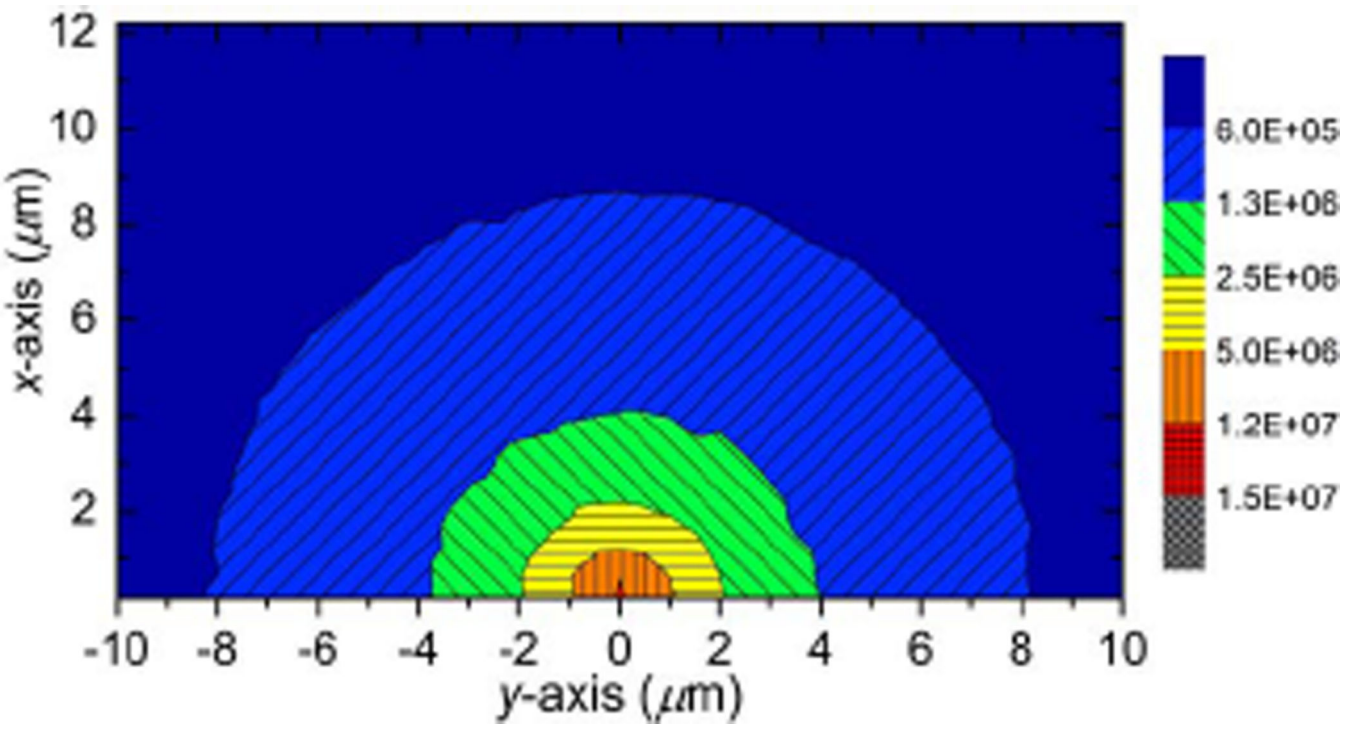

Fig. 3.

Simulated distribution of electric field intensity (unit: V/m) around the sensing zone (axis origin corresponds to the gap in Fig. 1(c)).

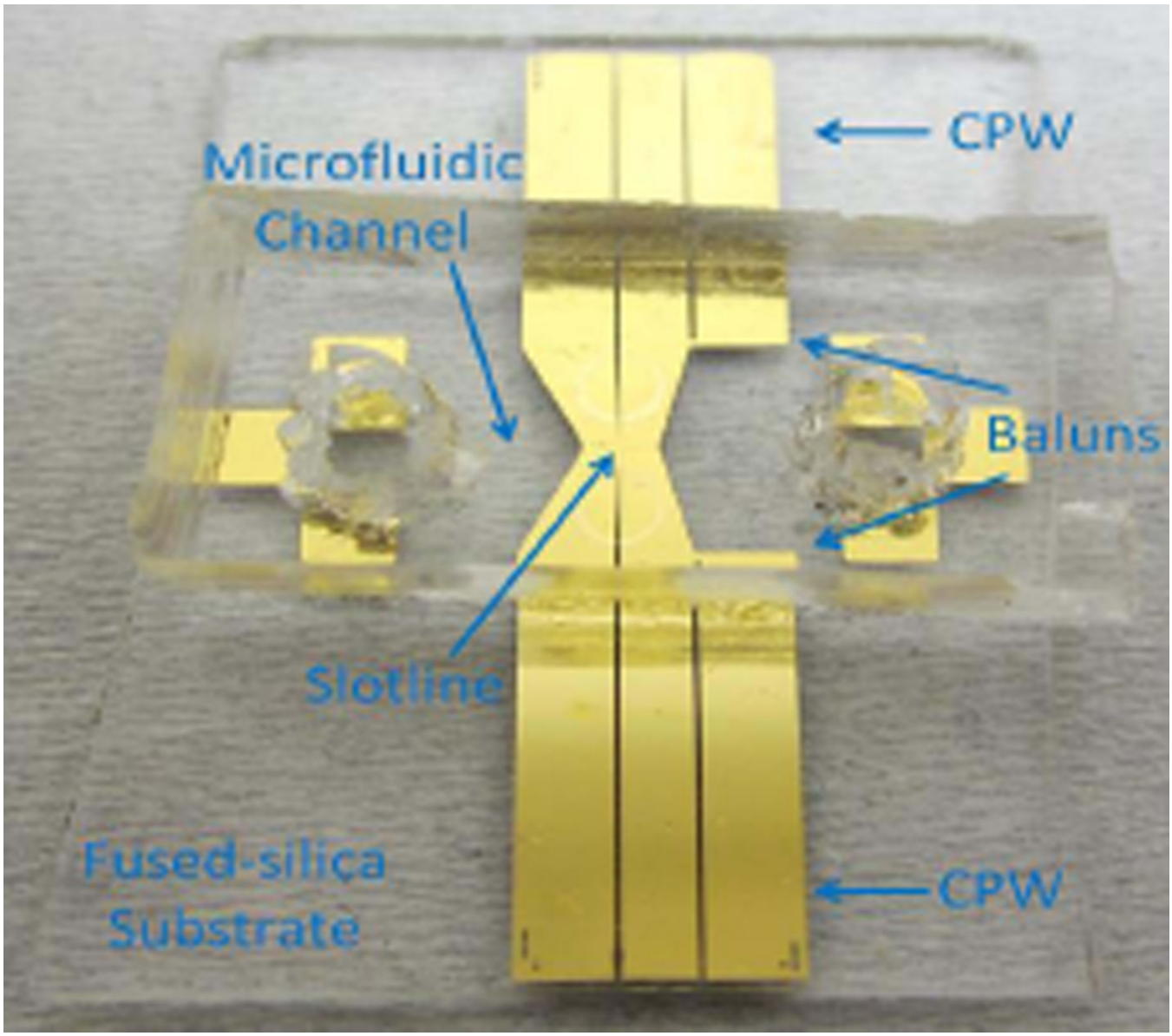

Fig. 4.
Slotline-based sensor with PDMS microfluidic channel.

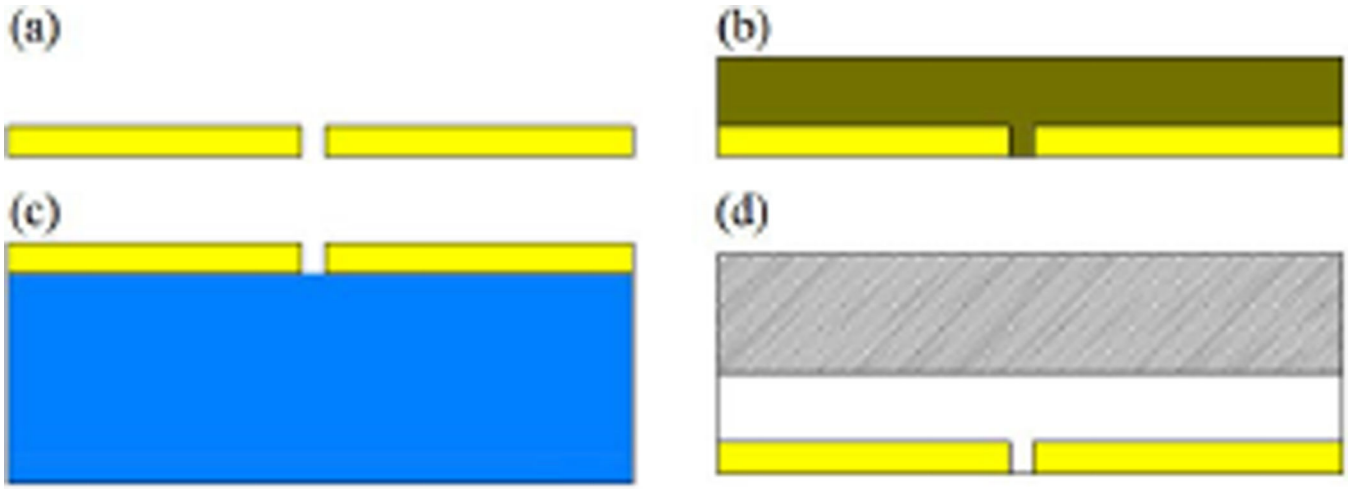

Fig. 5.
Configurations of partial capacitances: (a) C_{air}, (b) C_{carr}, (c) C_{sub}, and (d) C_{PDMS}.

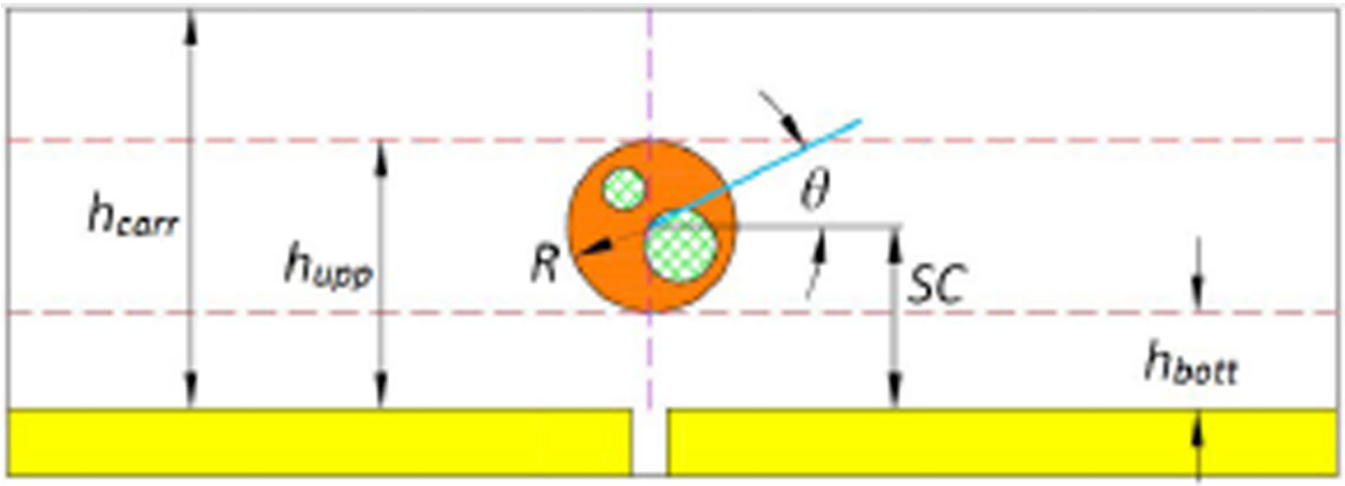

Fig. 6.

Partition of the carrier layer (horizontal dash line), and magnetic wall (vertical dash line) with single GUV (solid circle with two meshed circles marked as microdomains on it).

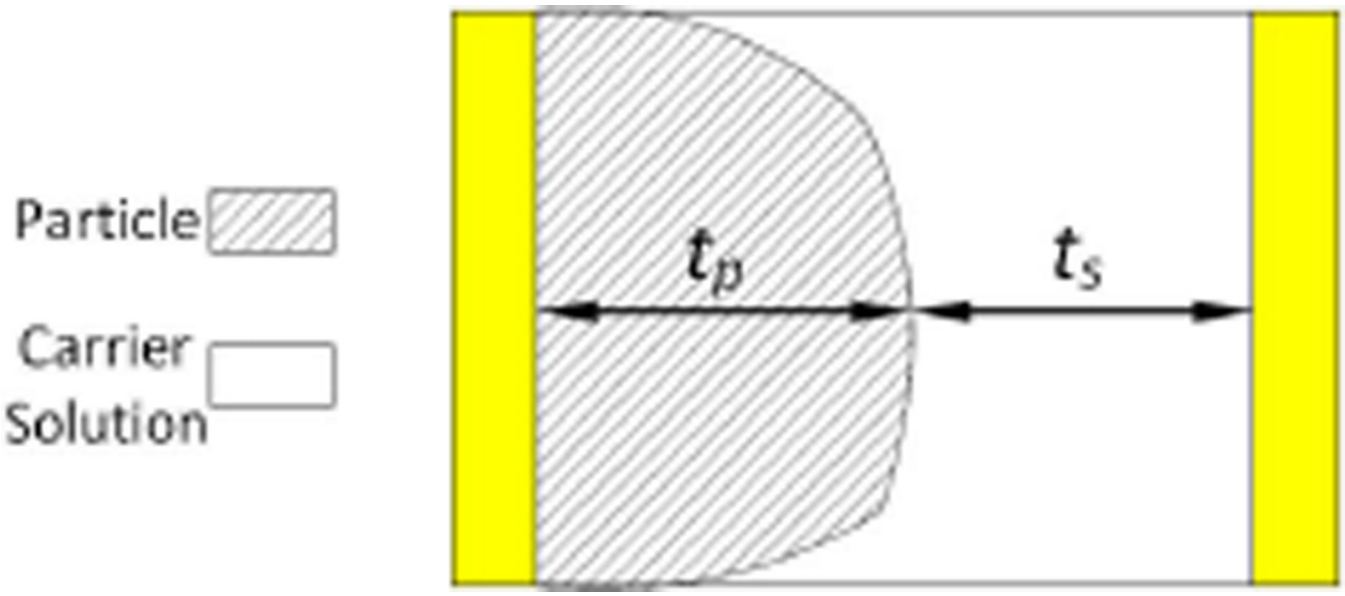

Fig. 7.
Two-dimensional conformal mapping of particle-solution layer (w plane).

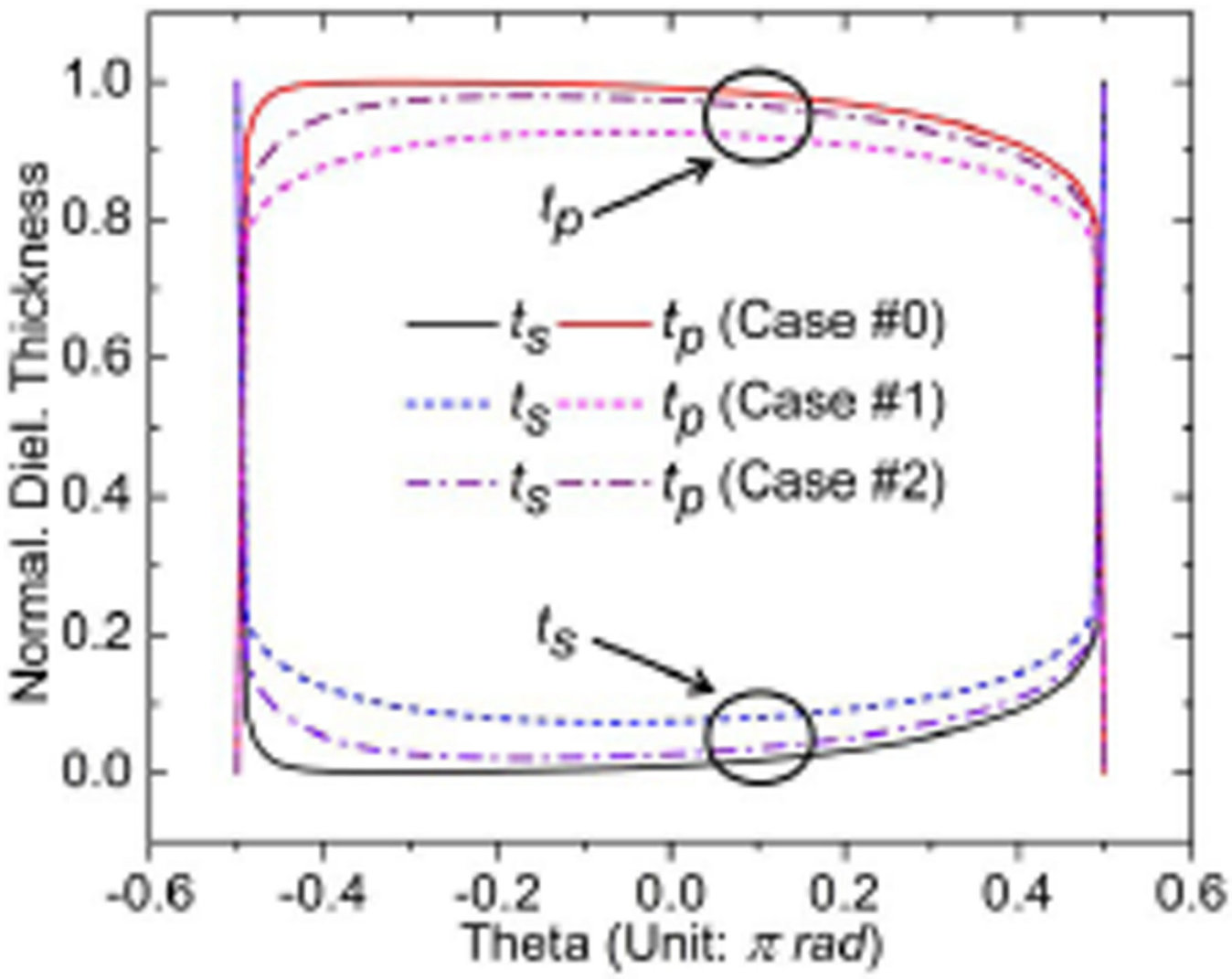

Fig. 8.

t_p and t_s versus θ for: case #0, w=100 nm, SC=6 μm, R=5 μm; case #1, w=100 nm, SC=15 μm, R=5 μm; case #2, w=100 nm, SC=20 μm, R=10 μm.

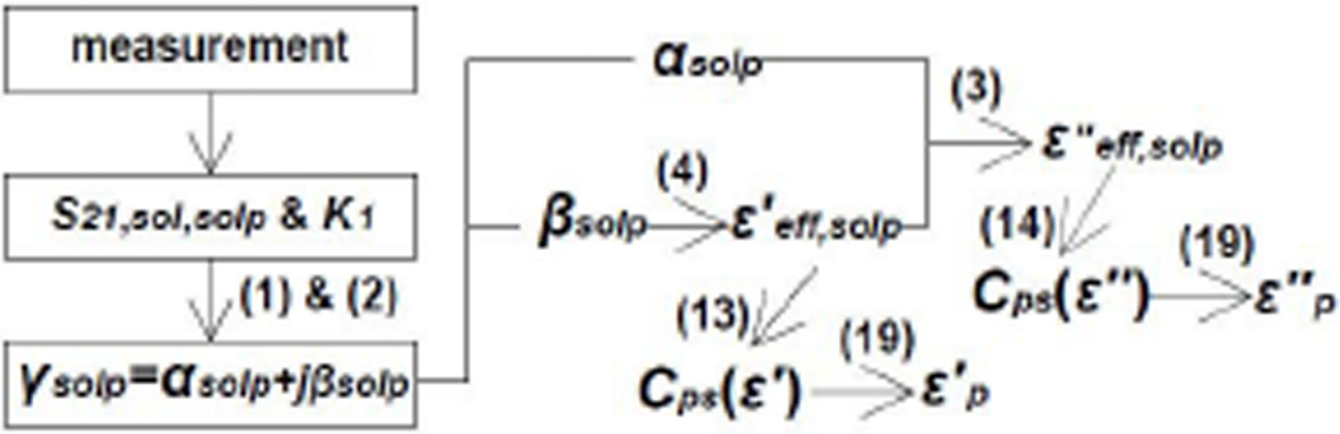

Fig. 9.
Algorithm to obtain GUV permittivity values from *S*-parameters.

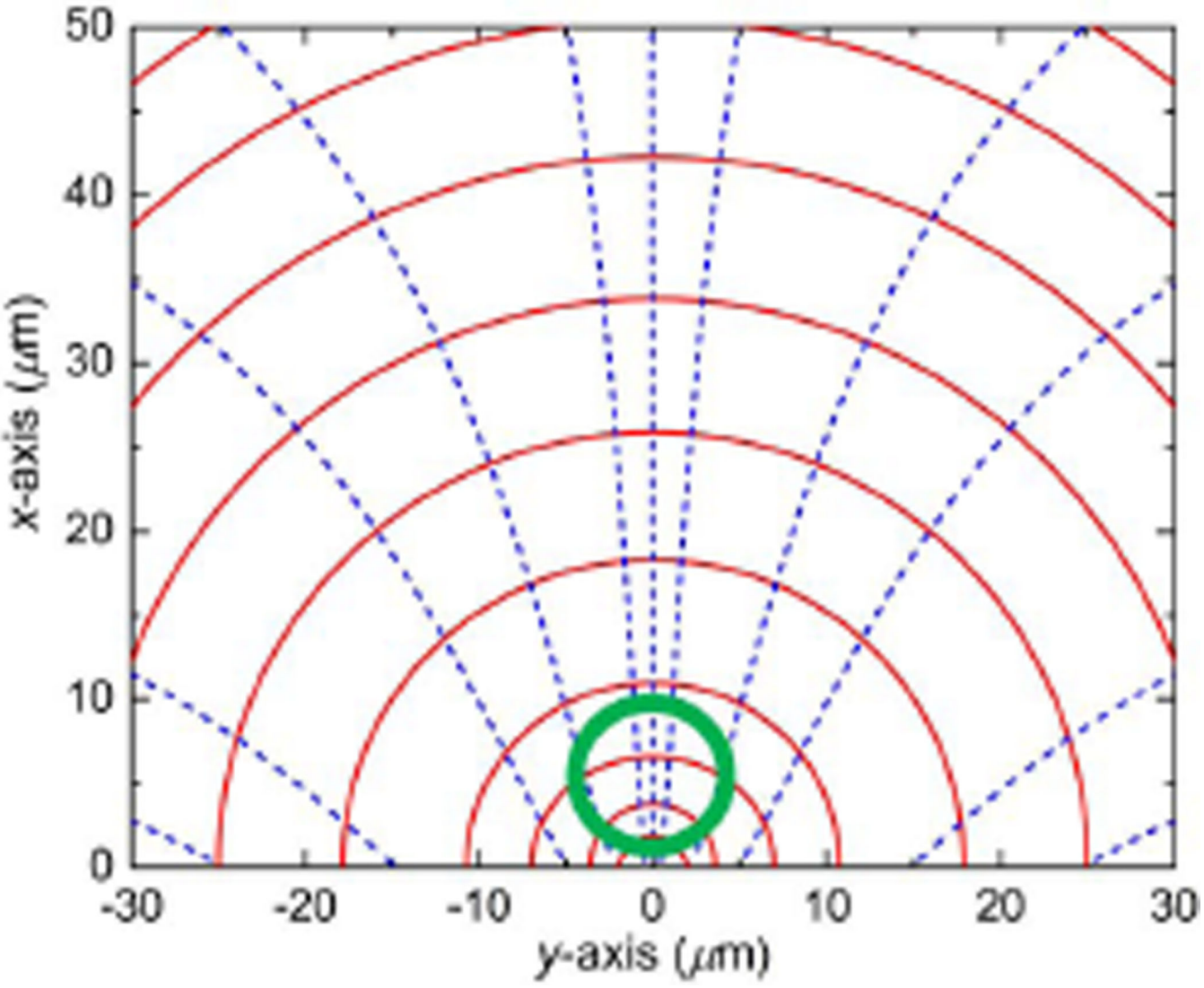

Fig. 10.

Cross-sectional distributions of EM fields. Red semi-circle clusters: electric field; blue parabola clusters: magnetic field. The bold green circle indicates the location of the GUV particle (*x*-*y* plane corresponding to the cross section in Fig. 1, and the origin is selected at the center of the gap).

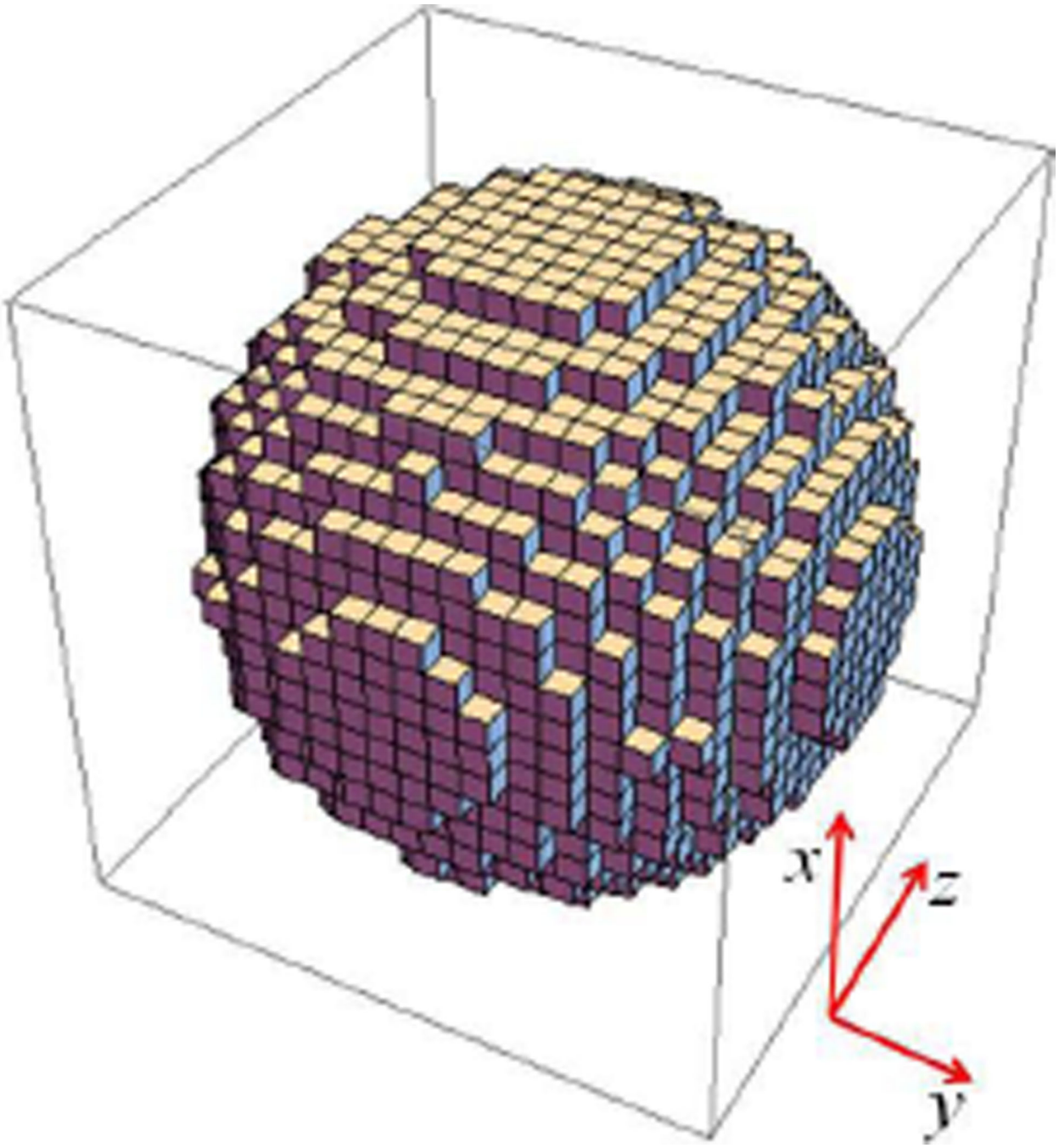

Fig. 11.

Approximating a 10 μm diameter sphere with 4,999 cubes (*x*-*y* plane corresponding to the cross section in Fig. 1).

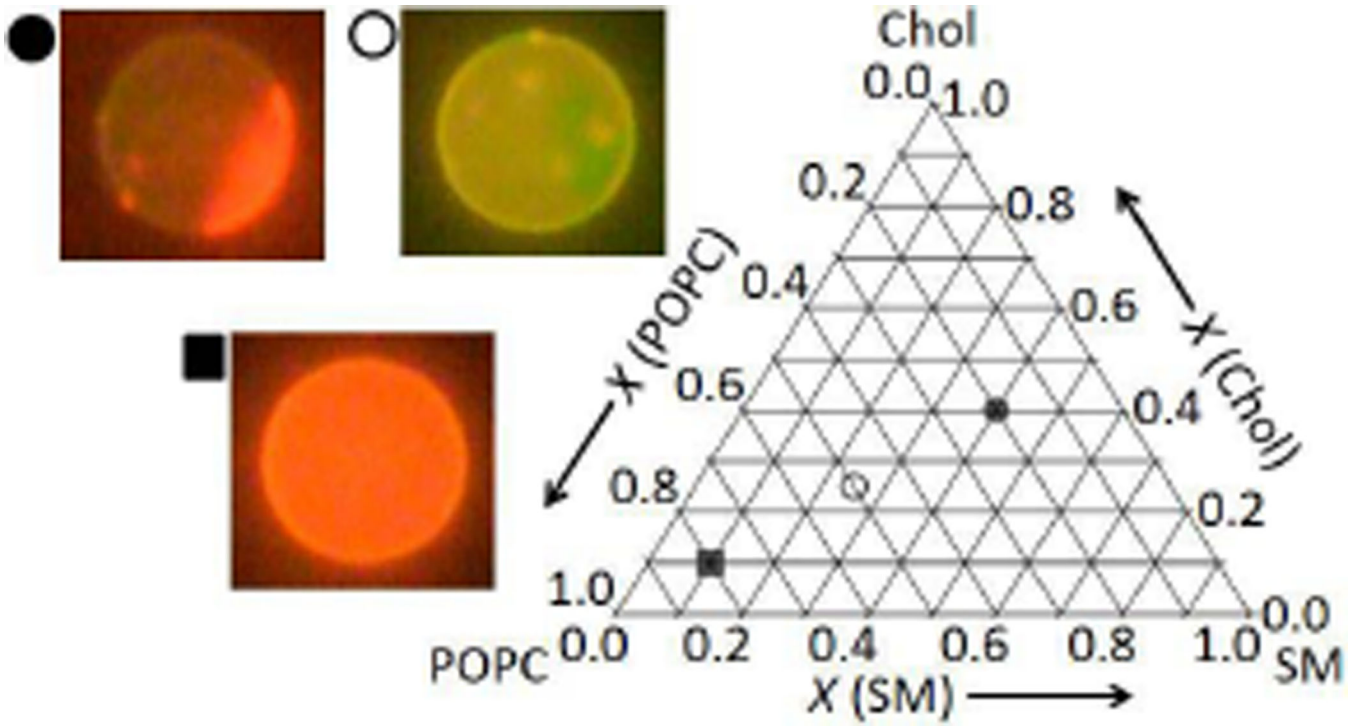

Fig. 12.

Images of synthesized GUVs at different molecular compositions POPC/SM/Chol shown on a ternary composition diagram (hollow circle, *I*: 2/1/1; solid circle, *II*: 1/2/2; solid square, *III*: 8/1/1). Liquid-disordered phase L_{α}: red; liquid-ordered phase L_{o}: green.

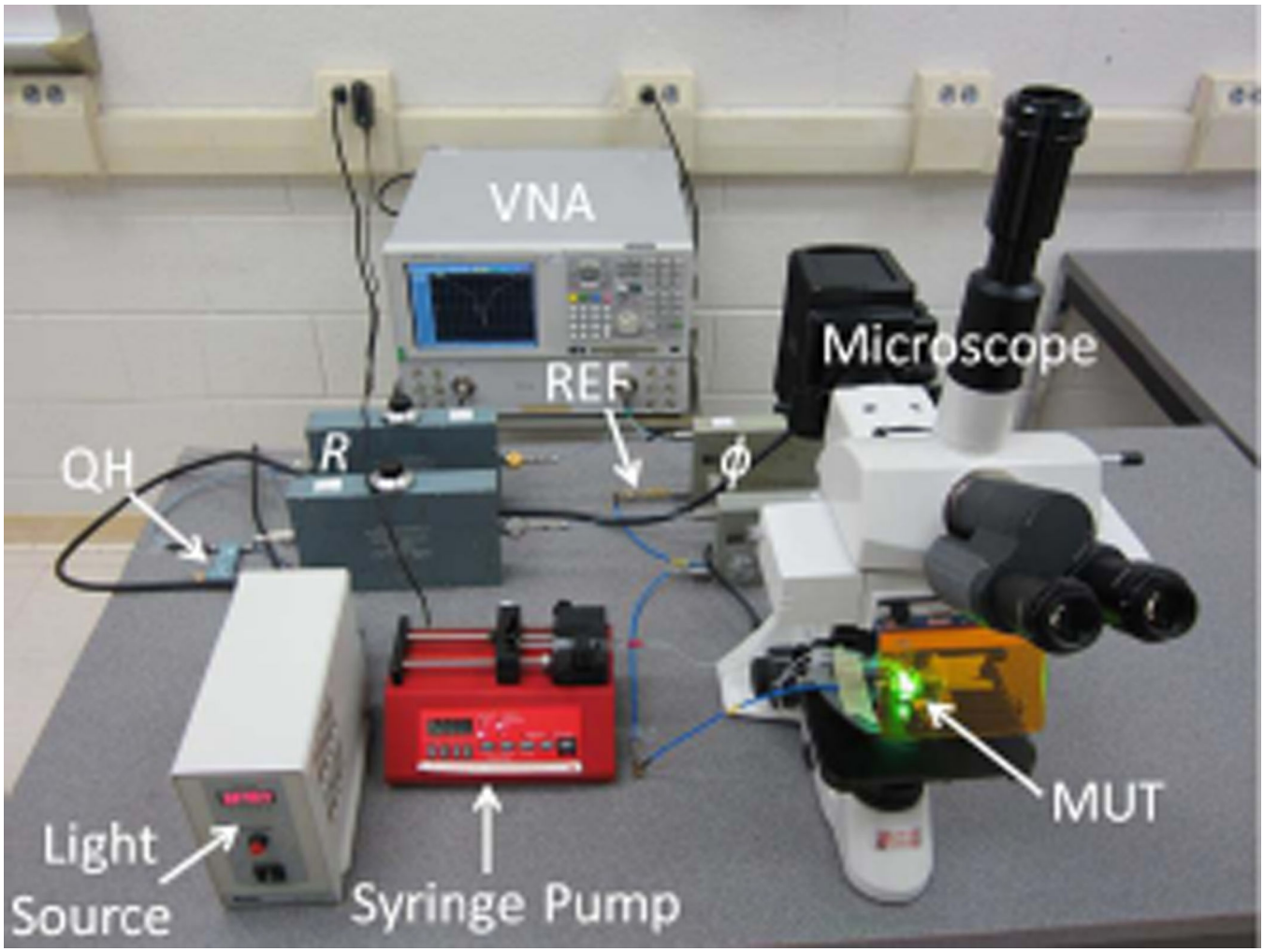

Fig. 13.
Measurement setup for single GUVs.

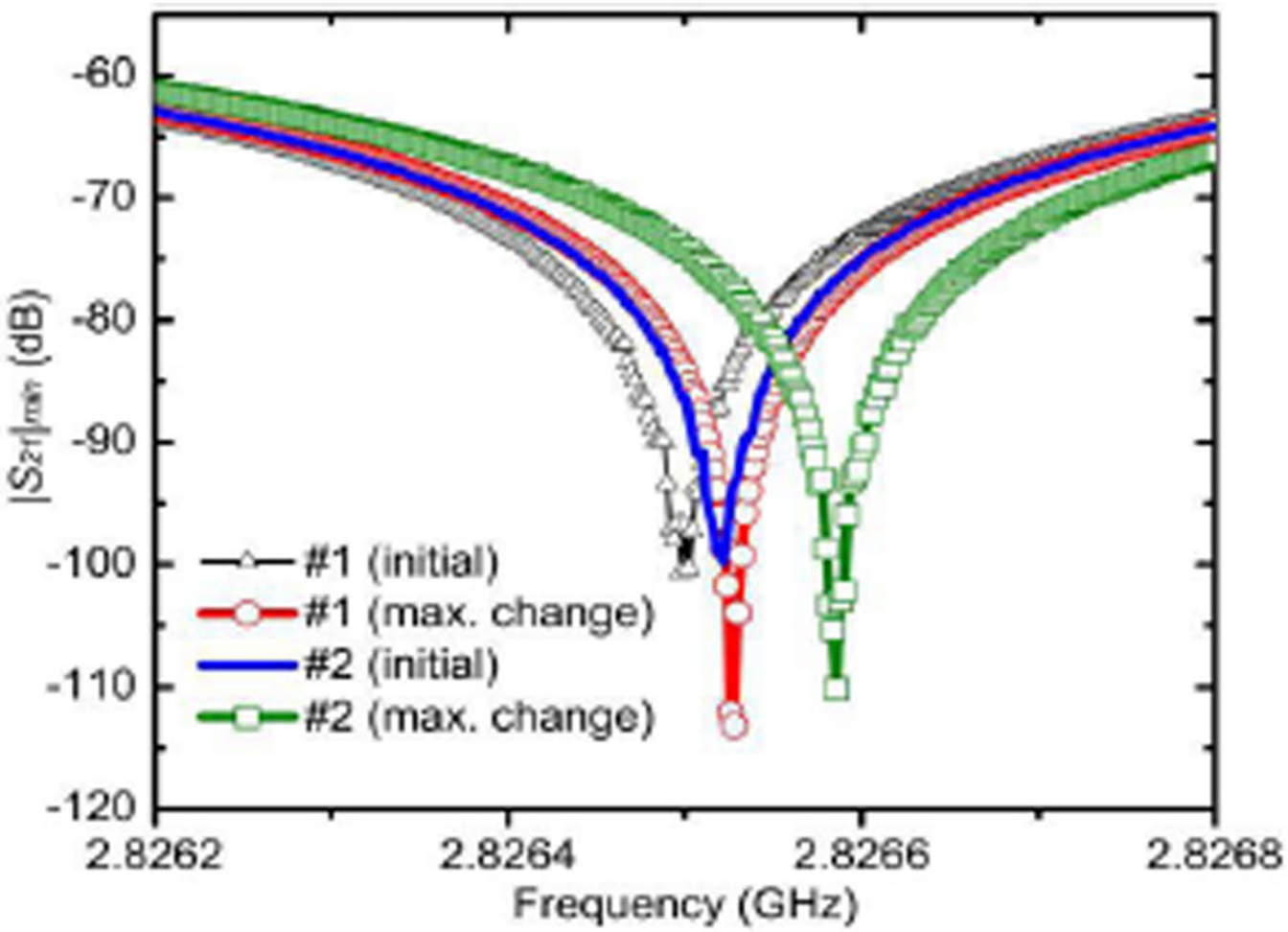

Fig. 14.
Measured $|S_{21}|$ for Group *1* at ~2.8 GHz.

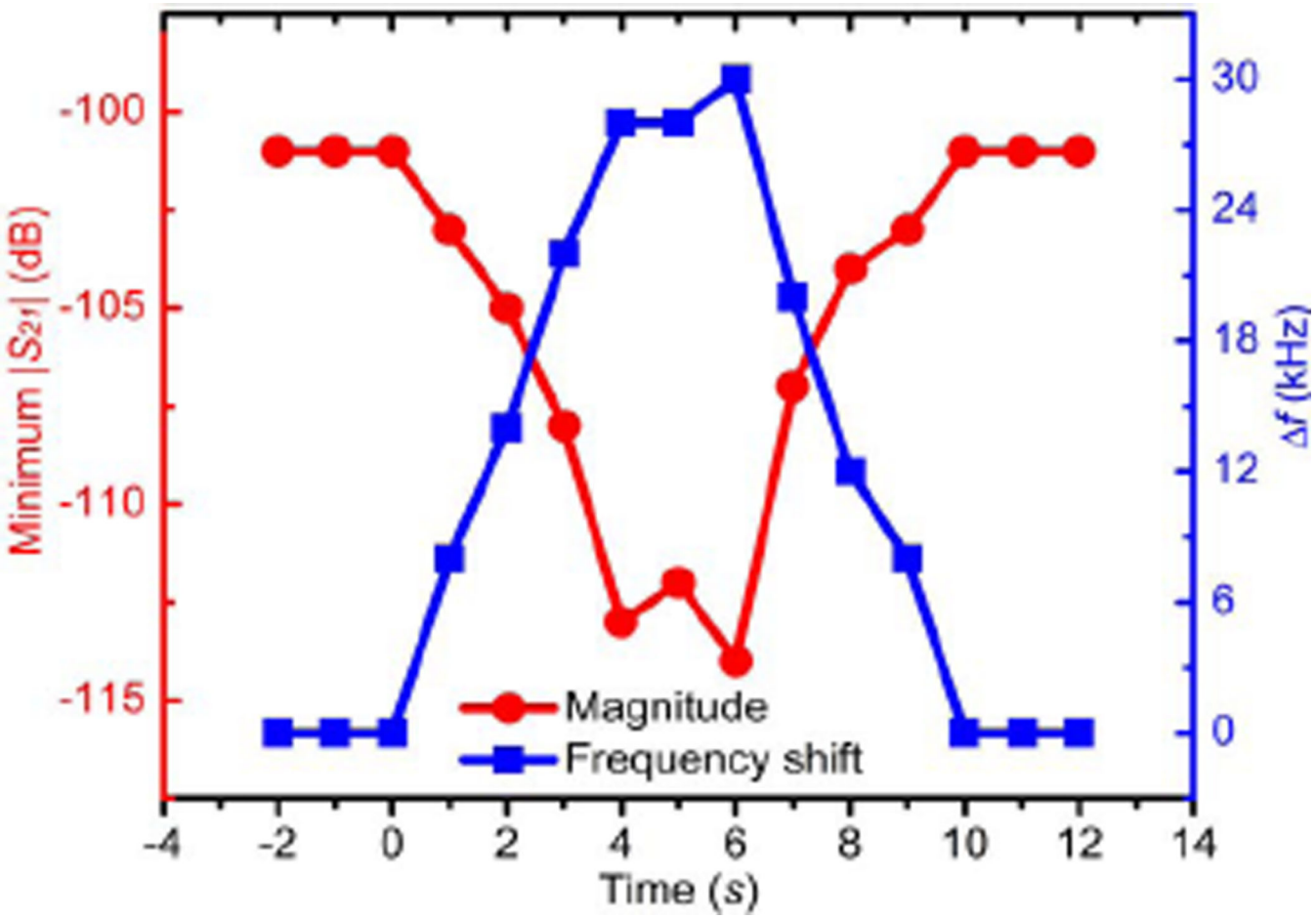

Fig. 15.

Time-dependent $|S_{21}|_{min}$ and corresponding Δf (f_0: ~2.8 GHz) when single GUV passing through the slotline gap.

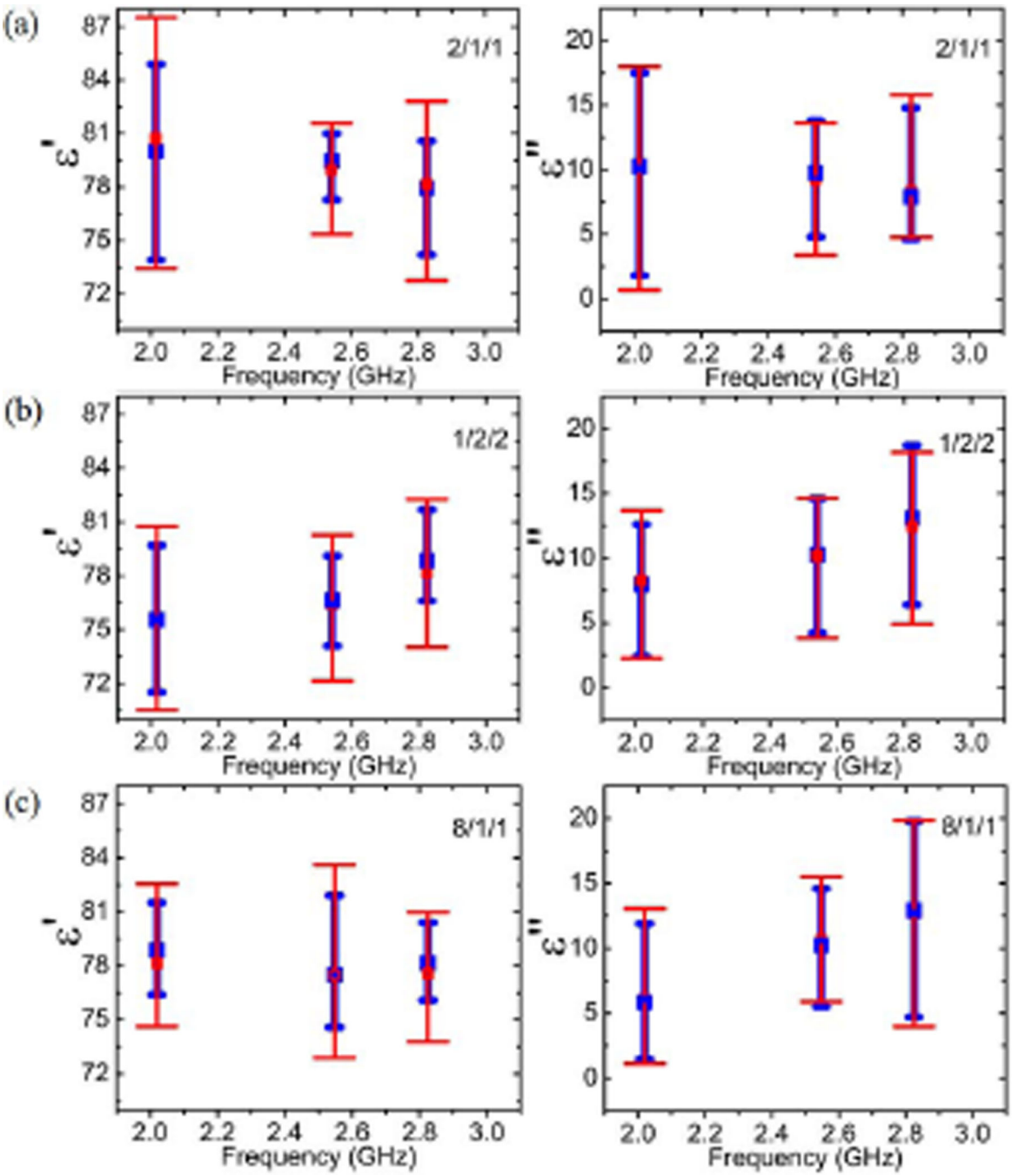

Fig. 16.

The obtained real and imaginary permittivities ε' and ε'', of GUV particles for (a) Group *I* (POPC/SM/Chol: 2/1/1), (b) Group *II* (POPC/SM/Chol: 1/2/2), and (c) Group *III* (POPC/SM/Chol: 8/1/1) at different frequencies (blue bold lines and small caps are for Model #1; red thin lines and big caps are for Model #2).

TABLE I

Parameters Used for Estimating $|S_{21}|_{min}$

Parameter	Symbol	Value
Thickness of PDMS	h_{PDMS}-h_{carr}	2 mm
Relative dielectric constant of PDMS	ε_{PDMS}	2.5
Thickness of substrate	h_{sub}	1 mm
Relative dielectric constant of substrate	ε_{sub}	3.75
Width of microfluidic channel	l_{sol}	50 μm
Height of microfluidic channel	h_{carr}	50 μm
Radius of GUV	R	5 μm
Spherical-center coordinate of GUV	SC	6 μm
Width of slotline gap	w	100 μm

TABLE II

Estimated Minimum Required $|S_{21}|_{min}$

$\mathbf{e}_p$	$\|S_{21}\|_{min}$ (dB)		
	Model #1	**Model #2**	**HFSS**
74.55−*j*11.84	−99.46	−106.99	−108.73
73.55−*j*12.84	−97.78	−102.55	−96.66
60−*j*25	−82.45	−86.78	−77.42
10−*j*1	−68.60	−77.04	−72.53

TABLE III

Extracted Permittivities at Different Times in Fig. 15

Time (*s*)	ϵ_p (Model #2)
1	79.41−*j*16.16
2	79.41−*j*16.16
3	79.41−*j*16.16
4	79.42−*j*16.15
5	79.42−*j*16.12
6	79.43−*j*16.08
7	79.40−*j*16.14
8	79.41−*j*16.15
9	79.41−*j*16.16

TABLE IV

Extracted Permittivities When Different *R*s, *SC*s, and h_{bott}s are Used (Unit: μm for *R*s, *SC*s, and h_{bott}s)

#	*R*	*SC*	h_{bott}	ε_p (Model #1)	ε_p (Model #2)
0	5	6	1	78.46−*j*14.46	79.43−*j*16.08
1	6	7	1	78.23−*j*14.56	79.10−*j*16.17
2	4	5	1	78.78−*j*15.93	79.91−*j*18.61
3	5	7	2	79.31−*j*15.89	80.89−*j*18.44
4	5	5.5	0.5	77.89−*j*15.68	77.30−*j*18.04
5	5	25	20	90.65−*j*25.05	93.10−*j*27.53
6	5	45	40	104.31−*j*44.58	106.91−*j*48.64
7	15	16	1	77.82−*j*14.37	78.71−*j*15.95
8	24	25	1	77.66−*j*14.19	78.53−*j*15.69

Note: The results from Model #2 are obtained with δ=0.0001 for four significant digits. The extracted GUV complex permittivities using the conformal mapping and perturbation method are close to each other, which further indicate that the assumptions of these methods are reasonable. No HFSS simulation was used to extract complex permittivities due to high computational cost.